Observation of dynamical quantum phase transitions in a spinor condensate

H.-X. Yang,[1] T. Tian,[1] Y.-B. Yang,[1] L.-Y. Qiu,[1] H.-Y. Liang,[1] A.-J. Chu,[1] C. B. Dağ,[2] Y. Xu,[1] Y. Liu,[3] and L.-M. Duan[1,*]

[1]*Center for Quantum Information, IIIS, Tsinghua University, Beijing 100084, People's Republic of China*

[2]*Department of Physics, University of Michigan, Ann Arbor, Michigan 48109, USA*

[3]*Department of Physics, Oklahoma State University, Stillwater, Oklahoma 74078, USA*

(Received 23 February 2019; published 17 July 2019)

A dynamical quantum phase transition can be characterized by a nonanalytic change in the quench dynamics when a parameter in the governing Hamiltonian is varied. Such a transition typically only shows up in long-time dynamics for extensive systems with short-range couplings. We analyze a model Hamiltonian of spin-1 particles with effectively infinite-range couplings and demonstrate that for this system the nonanalytic transition occurs for local observables in short-time durations even when the system is of a large size. We experimentally realize this model Hamiltonian and observe the dynamical quantum phase transition in an antiferromagnetic spinor Bose-Einstein condensate of around 10^5 sodium atoms. Our observations agree well with the theoretical prediction. We also analyze the scaling exponent near the dynamical phase transition and discuss its relation with the excited-state spectrum of the system.

DOI: 10.1103/PhysRevA.100.013622

I. INTRODUCTION

Nonequilibrium quantum many-body dynamics is intricate and largely awaiting exploration [1]. A dynamical quantum phase transition (DQPT) is a peculiar example of nonequilibrium many-body dynamics that has recently attracted significant interest [2–5]. Two different but related types of DQPTs have been defined in the literature [2–7]. A type I DQPT arises when the quench dynamics undergoes a nonanalytic change with respect to a system parameter in a quenched Hamiltonian [2–6]. In contrast, a type II DQPT appears when one global order parameter under the quench Hamiltonian has a nonanalytic singularity in its time evolutions (such as the Loschmidt echo) [2,4–10]. Observing DQPTs in systems with short-range couplings requires measurements of long-range correlations (e.g., infinite range in the thermodynamic limit for type II DQPTs) or asymptotic long-time dynamics (e.g., infinite time in the thermodynamic limit for type I DQPTs) [6,11]. Very recently, type I DQPTs have been observed in experiments satisfying a spin-1/2 Ising model with up to several tens of trapped ions [12] or Rydberg atoms [13], where the required observation time t is within the experimental reach because of the limited system size. As t scales up with the system size for type I DQPTs, it has been challenging to confirm DQPTs in large systems near the thermodynamic limit.

In this paper, we experimentally demonstrate the type I DQPT in a spinor Bose-Einstein condensate (BEC) with up to 10^5 sodium atoms. We start by analyzing a model Hamiltonian of spin-1 particles with effectively infinite-range couplings. Our results show that the infinite-range couplings cause type I DQPTs to occur in a finite and practically short-time duration even for a system in the thermodynamic limit, which largely simplifies their experimental observation. After experimentally realizing the model Hamiltonian, we observe type I DQPTs in an antiferromagnetic spinor BEC of around 10^5 sodium atoms, a massive system size compared with that in previous experiments [8,12,13]. Even in this large system size, we confirm that the DQPTs still occur in short-time properties of the quench dynamics. We also measure the scaling critical exponents of the order parameters near the DQPTs and find that they are close to the theoretical prediction.

II. THEORETICAL PREDICTION

A model Hamiltonian of N spin-1 particles with effectively infinite-range (all-to-all) couplings takes the form

$$\hat{H} = \frac{c_2}{2N} \sum_{1 \leqslant i,j \leqslant N} \mathbf{S}_i \cdot \mathbf{S}_j + \sum_{1 \leqslant i \leqslant N} \left(q S_{iz}^2 - p S_{iz} \right), \qquad (1)$$

where $\mathbf{S}_i$ is the spin-1 operator for the ith particle, with its z component denoted S_{iz}, c_2 is the spin-dependent interaction, which is positive for antiferromagnetic spinor BECs, and $p(q)$ denotes the linear (quadratic) Zeeman energy, respectively. For infinite-range coupling, the spin coupling rate is normalized as $c_2/(2N)$ so that the energy is extensive under the thermodynamic limit ($N \to \infty$) with a finite c_2.

We realize this model Hamiltonian with a BEC of N spin-1 atoms. The spatial coherence over the whole BEC gives effectively infinite-range coupling between the atomic spin operators, although the atomic collision interaction by itself is fully local. The single-spatial-mode approximation (SMA) is widely used to describe spinor BECs. The SMA decomposes the atomic field operator as $\hat{\Psi}_i(\mathbf{r}) \simeq \Phi(\mathbf{r})\hat{a}_i$ by assuming that all spin states have the same spatial wave function $\Phi(\mathbf{r})$ and $\hat{a}_i$ is the annihilation operator for the ith spin component. The

*lmduan@tsinghua.edu.cn

Hamiltonian for spin-1 BECs under the SMA is thus [14,15]

$$\hat{H} = c_2 \frac{\hat{L}^2}{2N} + \sum_{m=-1}^{1} (qm^2 - pm)\hat{a}_m^\dagger \hat{a}_m, \tag{2}$$

where $\hat{L}_\mu = \sum_{m,n} \hat{a}_m^\dagger (f_\mu)_{mn} \hat{a}_n$ is the BEC's total spin operator (f_μ is the spin-1 angular momentum matrix). Note that Eq. (2) is exactly the second-quantization form of Eq. (1) with $\hat{L} \equiv \sum_{i=1}^{N} \hat{\mathbf{S}}_i$ under the Schwinger representation of the spin operators.

Spinor BECs have been used to study quantum magnetism, spin squeezing, and nonequilibrium dynamics [14–18]. Here, we use them as an experimental platform to study DQPTs under an effectively infinite-range coupling model as described by Eq. (1). We start from an initial state $|\psi(0)\rangle$ of the model Hamiltonian by preparing all the atoms on the hyperfine level $|F = 1, m_F = 0\rangle$ with $L_z = 0$, and the system remains in the $L_z = 0$ subspace since the total magnetization L_z is a conserved operator in this model. The linear Zeeman term thus makes no contribution to the dynamics and can be neglected. The interplay between the spin-interaction term and the quadratic Zeeman term gives interesting spin-mixing dynamics [19]. We set the initial q at a value $q_i \gtrsim c_2$ so that $|\psi(0)\rangle$ is the ground state of Eq. (2). We then suddenly quench q to a final value q_f. As q_f is scanned continuously, a sudden change in the quench dynamics at q_c can be regarded as a signature of the DQPT.

Convenient detectable signals in spinor BECs are the fractional population of the spin-m_F component ($\rho_{m_F} = \hat{a}_{m_F}^\dagger \hat{a}_{m_F}/N$) and its average value ($\overline{\rho_{m_F}} = \langle \hat{a}_{m_F}^\dagger \hat{a}_{m_F} \rangle / N$) derived from repeated measurements. And a widely used quantity for characterizing the quench dynamics is $\langle \overline{\rho_0} \rangle_\infty$, the long-time average of $\overline{\rho_0}(t)$ after the quench. By assuming that the quench occurs at $t = 0$, we can define $\langle \overline{\rho_0} \rangle_\infty = \lim_{T\to\infty} \frac{1}{T} \int_0^T \overline{\rho_0}(t)dt$ [6,11,18]. Using $\langle \overline{\rho_0} \rangle_\infty$ as a measure, Ref. [18] shows that the model Hamiltonian [Eq. (1) or Eq. (2)] supports a DQPT at $q_f = 0$. The quantity $\langle \overline{\rho_0} \rangle_\infty$, however, is difficult to measure experimentally as it requires averaging over a long evolution time t (i.e., $t \to \infty$ is theoretically required for a system in the thermodynamic limit). For spinor BECs, a large t inevitably leads to several challenges, such as significant atom losses and invalidity of the SMA [19–21], which all hinder experimental observations of DQPTs.

To overcome this problem, we propose to identify DQPTs using different parameters, which can be directly measured within short-time evolutions and correlate unambiguously with $\langle \overline{\rho_0} \rangle_\infty$. To simulate the quench dynamics, we numerically diagonalize the model Hamiltonian, (2), in the Fock basis $|N_1, N_0, N_{-1}\rangle = |n, N-2n, n\rangle$. After quenching q to q_f, we find that $\overline{\rho_0}(t)$ first displays some oscillations. We define a quantity $A_{\rm dip} \equiv 1 - \overline{\rho_0}(t = \tau_{\rm dip})$, with $\overline{\rho_0}(t = \tau_{\rm dip})$ being the value of $\overline{\rho_0}(t)$ at the first dip of the spin oscillations. By numerically solving the model Hamiltonian, we demonstrate that the dip depth $A_{\rm dip}$ is a good measure of DQPTs. A typical simulation result extracted from the quench dynamics at $N \sim 1 \times 10^5$ is shown in Fig. 1, which clearly indicates that the behaviors of $\langle \overline{\rho_0} \rangle_\infty$ and $A_{\rm dip}$ are strongly correlated and they have nonanalytic sudden jumps at exactly the same q_f, marking a first-order DQPT at $q_f = q_c = 0$. For systems

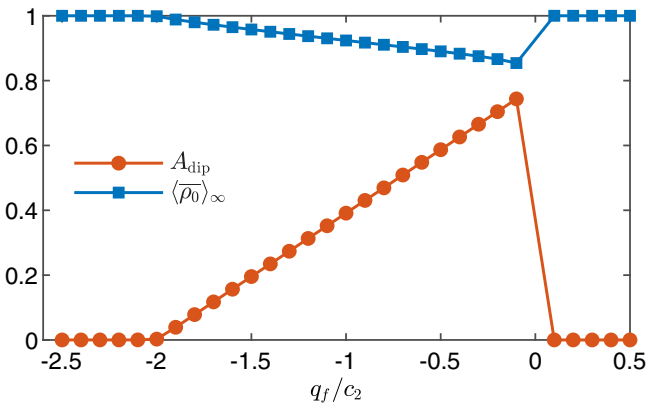

FIG. 1. Predicted $A_{\rm dip}$ (depth of the first dip in spin oscillations) and long-time average $\langle \overline{\rho_0} \rangle_\infty$ as functions of q_f/c_2 for $N = 1 \times 10^5$ and $q_i = 0.5c_2$ (see text). It appears that the short-time property $A_{\rm dip}$ and the long-time property $\langle \overline{\rho_0} \rangle_\infty$ both signal DQPTs at the same q_f.

with short-range couplings, the signature of DQPTs only shows up in long-time evolutions of local quantities, as the interaction effect needs to propagate over the system size. This argument is not valid for our model Hamiltonian, as it has effectively infinite-range all-to-all couplings. This explains why the short-time quantity $A_{\rm dip}$ and the conventional long-time quantity $\langle \overline{\rho_0} \rangle_\infty$ mark the DQPTs equally well. In contrast to $\langle \overline{\rho_0} \rangle_\infty$, $A_{\rm dip}$ can be easily and precisely measured, because the dip time $\tau_{\rm dip}$ is short enough to avoid detrimental changes induced by long-time evolutions.

III. EXPERIMENTAL RESULTS AND DISCUSSION

We produce a spin-1 BEC of 1.3×10^5 sodium atoms via an all-optical procedure similar to that in Ref. [22]. A longitudinal polar (LP) state with $\overline{\rho_0} = 1$ is chosen as the initial state, because it is the ground state of the model Hamiltonian at $q_i/h = 42.3$ Hz, with h being the Planck constant. To fully polarize atoms to the $|F = 1, m_F = 0\rangle$ state, we hold the BEC under a large magnetic field gradient for 5 ms to eliminate the $|m_F = \pm 1\rangle$ atoms [23]. We then slowly turn off the gradient, in 50 ms, and hold the atoms for another 300 ms to sufficiently equilibrate the system. This method efficiently produces an LP state of up to 1×10^5 atoms.

In this paper, DQPTs are observed after a sudden quench of the quadratic Zeeman energy q. Similarly to Refs. [24–26], we tune q via a microwave dressing field, i.e., $q = q_B + q_M$, with q_B (q_M) representing the quadratic Zeeman energy induced by a magnetic field (a microwave dressing field). The value of q_B is always positive for antiferromagnetic spin-1 sodium BECs, while q_M can be tuned to any value from $-\infty$ to $+\infty$ simply by changing the frequency or the intensity of applied microwave pulses [24].

To probe the quench dynamics, after the initial LP state preparation at q_i in a fixed magnetic field, we suddenly turn on a microwave dressing field to abruptly change q_i to $q_f = q_i + q_M$. After holding spinor gases at q_f for a given time t, we measure the fractional populations ρ_{m_F} via the standard Stern-Gerlach absorption imaging technique. To experimentally determine $\overline{\rho_0}(t)$, we repeat the same experiments 80 times and

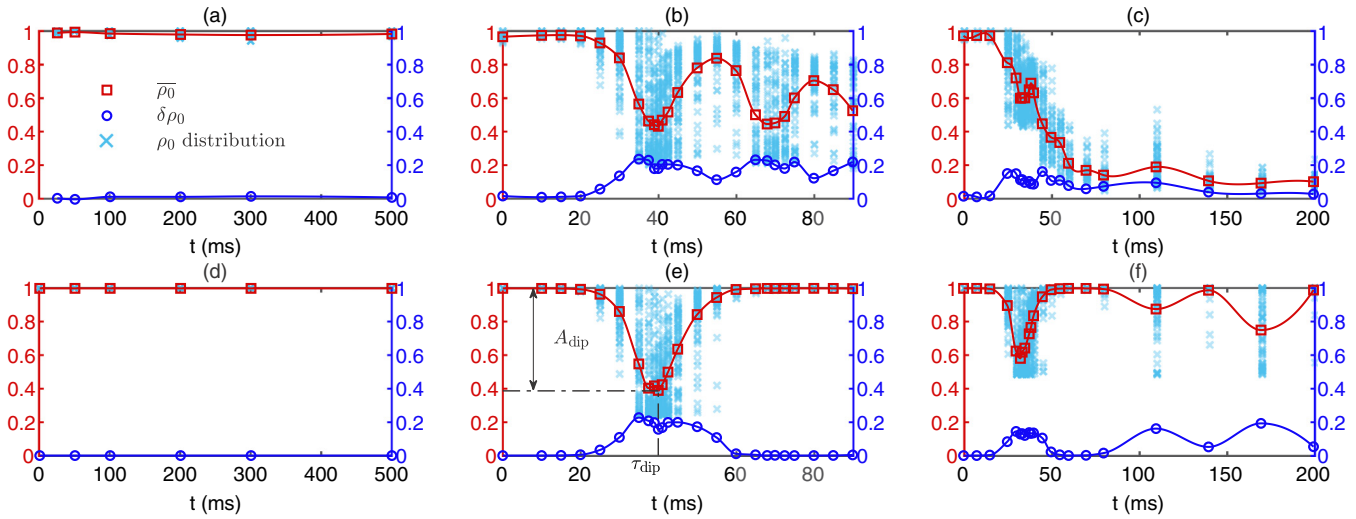

FIG. 2. Observed time evolutions of $\overline{\rho_0}$ and corresponding theoretical predictions derived from numerical simulations of the quench dynamics at three q_f/c_2 values (see text). (a, b, c) Experimental results at $c_2/h = 31$ Hz and $q_f/c_2 = 0.65,\ -0.48$, and -0.97, respectively. (d, e, f) Numerical simulations at $q_f/c_2 = 0.65,\ -0.48$, and -0.97, respectively. We repeat the experiments and simulations 80 times under each condition. The blue crosses in the background show the measurement results from these repeated experiments (upper panel) or Monte Carlo simulations (lower panel). Red squares denote the average value $\overline{\rho_0}(t)$ from these 80 trials of measurements and blue circles denote the corresponding standard deviations.

measure the whole evolution $\rho_0(t)$ for every repetition. The time evolution of ρ_0 from each of these 80 repeated experiments, as well as their mean value $\overline{\rho_0}(t)$ and the standard deviation $\delta\rho_0(t)$, are shown in Figs. 2(a)–2(c) for three typical q_f values. Note that the large variation in the observed ρ_0 at certain q_f and t for different rounds of experiments is not due to experimental imperfection, but an intrinsic feature of the quench dynamics related to the DQPTs. At this q_f and t, the dynamical state is far from the ground state and involves a superposition of many eigenstates of the Hamiltonian, so ρ_0 has large intrinsic quantum fluctuations. To put this experimental result into context, we also numerically calculate the time evolution under the model Hamiltonian, (2), and the corresponding results are shown in Figs. 2(d)–2(f). To compare theory and experiments, we also show the theoretical distribution of ρ_0 under 80 repetitions of measurements using Monte Carlo sampling. Through numerical diagonalization of model Hamiltonian (2), we obtain the theoretical probability distribution of ρ_0, labeled $f(\rho_0)$, under certain q_f and t. We numerically sample ρ_0 80 times based on $f(\rho_0)$. This operation mimics the experimental procedure.

The time evolution of $\overline{\rho_0}$ shows qualitatively different behaviors in three regions of q_f. When $q_f > 0$ as shown in Figs. 2(a) and 2(d), $\overline{\rho_0}(t)$ always stays very close to 1 with a negligible variation $\delta\rho_0(t)$. The experimental results appear to agree very well with theory in this region. When q_f/c_2 is negative but not too small [Figs. 2(b) and 2(e)], $\overline{\rho_0}(t)$ begins to oscillate and the $\rho_0(t)$ distribution shows quite large fluctuations. The experimental results coincide with the theoretical prediction in the short-time region of $t \lesssim \tau_{\rm dip}$ but deviate significantly during the subsequent evolution. We attribute this to the breakdown of the SMA for the atomic motional state: the atoms in this case are in significantly excited states of the spin Hamiltonian and their energy can relax to the motional state through spin-dependent collisions and thus invalidate the prediction from the single-mode Hamiltonian, (2), in long-time dynamics. When q_f/c_2 gets more deeply into the negative region [Figs. 2(c) and 2(f)], although the theory based on Eq. (2) still predicts oscillations, the energy relaxation to the motional state dominates in experiments. The spin state approaches the transverse polar state with $\overline{\rho_0} = 0$, the ground state of the Hamiltonian at this negative q_f, through the relaxation; and spin oscillations are barely visible in quench dynamics for this case. The above observations show that it is important to detect the DQPTs by signals at short evolution times and keep q_f in a region not too far from the DQPT point at $q_c = 0$.

As elaborated in Fig. 1, we identify DQPTs with the signal at the first dip of $\overline{\rho_0}(t)$ [e.g., dip depth $A_{\rm dip}$ and standard deviation $\delta\rho_0(t)$ at $t = \tau_{\rm dip}$]. Figure 3 shows the observed

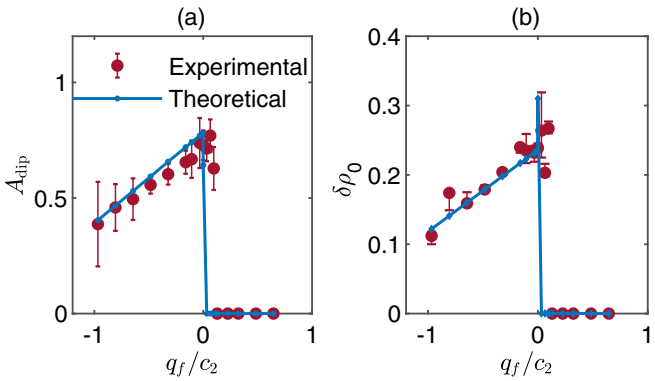

FIG. 3. Observed signatures of DQPTs. (a) Measured $A_{\rm dip}$ versus q_f/c_2. (b) Standard deviation $\delta\rho_0$ at $t = \tau_{\rm dip}$ versus q_f/c_2 at $c_2/h = 31$ Hz. Circles with error bars denote the experimental data and solid lines represent the theoretical results from numerical simulations of the model Hamiltonian (see text).

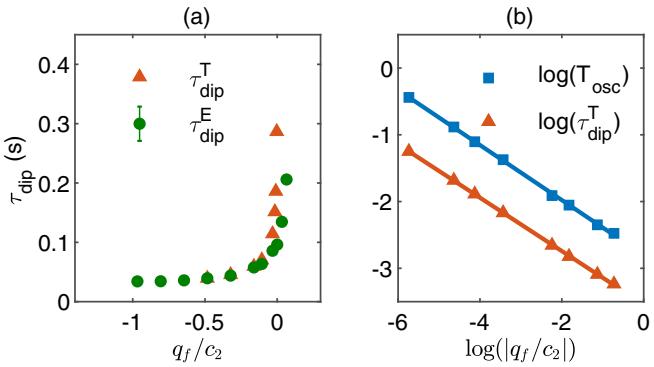

FIG. 4. (a) Circles (triangles) represent the observed occurrence time of the first dip (the corresponding theoretical result derived from numerical simulations) as a function of q_f/c_2 at $c_2/h = 31$ Hz. (b) Power-law scaling of the theoretical dip time τ^T_{dip} and T_{osc} (the inverse of the relevant energy gap) in a log-log diagram. The extracted critical exponents for T_{osc} and τ^T_{dip} are, respectively, -0.41 and -0.40, based on linear fits (denoted by solid lines) to the log-log curves.

A_{dip} and $\delta\rho_0(t = \tau_{dip})$ as a function of q_f after the system is quenched from the positive q_i to various negative (positive) q_f values with (without) crossing the DQPT point of $q_c = 0$. The results in Figs. 3(a) and 3(b) unambiguously confirm a first-order DQPT in our experimental system, with a sudden jump of A_{dip} and $\delta\rho_0$ at $q_f = q_c = 0$. When q_f is positive, both A_{dip} and $\delta\rho_0$ remain almost at 0. Across the DQPT transition point of $q_c = 0$, A_{dip} and $\delta\rho_0$ jump to significant finite values and these values gradually decrease by a linear scaling with $|q_f - q_c| = |q_f|$ when q_f is pushed to the negative region. The observed data agree very well with the theoretical prediction derived from the model Hamiltonian up to the experimental uncertainty of q_f, which is about $h \times 2.5$ Hz near $q = 0$ Hz. This demonstrates the major claim of our paper. With the measured linear scaling of A_{dip} with $|q_f|$ in the negative-q region, its critical exponent is found to be 1, in agreement with the result from numerical simulations. The theoretical origin of this dynamical critical exponent and its connection with the critical exponents for the equilibrium phase diagrams are interesting questions worthy of further investigation in future [27].

Another important observable worth noting is the occurrence time τ_{dip} of the first dip. In Fig. 4(a), we compare the observed dip time τ^E_{dip} with the theoretical τ^T_{dip} predicted by the model Hamiltonian. When q_f is very close to the DQPT point, the measured τ_{dip} is sensitive to the experimental calibration error on q_f, and there is some discrepancy between τ^E_{dip} and τ^T_{dip}. Apart from this small region, the measured τ_{dip} agrees quite well with the theoretical prediction. The theoretical dip time τ^T_{dip} also shows an interesting power-law scaling with $|q_f|$. To see this clearly, Fig. 4(b) displays τ^T_{dip} as a function of $|q_f|$ in a log-log plot. To understand the origin of the power-law scaling shown in Fig. 4(b), we note that although the quench dynamics involves the contribution of the whole energy spectrum, there are only a few energy eigenstates which play a dominant role when q_f is quenched across the DQPT point. Similarly to Ref. [18], we define the overlap function as a measure of the matrix element of ρ_0 in the

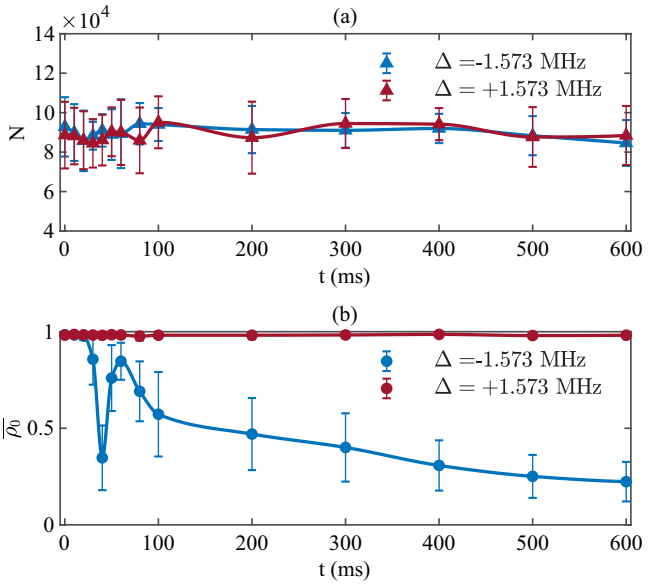

FIG. 5. Time evolutions of (a) N and (b) $\overline{\rho_0}$ observed in contrast experiments with two carefully chosen microwave pulses at $c_2/h = 34$ Hz. The two pulses have the same intensity but opposite frequency detunings of $\Delta = \pm 1.573$ MHz, which induce different microwave dressing fields of $q_f/c_2 = -0.36$ for $\Delta = -1.573$ MHz and $q_f/c_2 = 2.53$ for $\Delta = +1.573$ MHz.

basis composed of the eigenstates of the final Hamiltonian and δE as the nearest-neighbor energy gap at the maximum off-diagonal term of this overlap function. We then numerically calculate the main frequency component in the oscillation of $\overline{\rho_0}$, which turns out to be $\delta E/h$. The time scale, defined by $T_{osc} = h/\delta E$, also shows a power-law scaling with $|q_f|$. Figure 4(b) shows both T_{osc} and τ^T_{dip} as a function of $|q_f|$ in the log-log diagram, which clearly indicates that the two log-log curves have similar slopes. The extracted power-law scaling exponents are -0.41 for T_{osc} and -0.40 for τ^T_{dip}, through linear fits to the log-log curves in Fig. 4(b). This implies that the property of τ_{dip} is mainly determined by δE in the energy spectrum.

For an experiment performed in microwave dressing fields, atom losses induced by microwave pulses may not be negligible. To exclude the possibility that the spin oscillations shown in Fig. 2 are induced by trivial effects of microwave pulses, we conduct contrast experiments with two carefully chosen microwave pulses. The two microwave pulses have exactly the same intensity but opposite frequency detunings, i.e., their frequencies are detuned by $\pm\Delta$ from the transition from $|F = 1, m_F = 0\rangle$ to $|F = 2, m_F = 0\rangle$. Therefore, the trivial effects of microwave pulses on spin populations should be the same in these two cases. Figure 5 shows the observed time evolutions of the total atom number N and $\overline{\rho_0}$ immersed in these two different microwave pulses. It appears that N stays almost the same [Fig. 5(a)], with a negligible atom loss over the experimental time scale of a few hundreds of milliseconds, in the two cases. The observed time evolutions of $\overline{\rho_0}$ [Fig. 5(b)] are, however, very different in the two cases. This confirms that the detected $\overline{\rho_0}$ strongly depends on the actual strength of the applied microwave dressing field and is indeed introduced by the quench dynamics.

IV. CONCLUSION

In summary, we have unambiguously observed a dynamical quantum phase transition associated with an interacting model Hamiltonian of spin-1 particles with effectively infinite-range couplings. Due to the all-to-all couplings, we show that the DQPTs can be clearly identified by short-time dynamical properties of local observables, which enables its detection in a large spinor condensate, saving it from the complication of long-time relaxation dynamics inevitable in open quantum many-body systems. This experimental observation may open new prospects to study dynamical quantum phase transitions and their associated critical properties in cold atomic gases with engineered many-body Hamiltonians.

ACKNOWLEDGMENTS

This work was supported by the Ministry of Education of China and the National Key Research and Development Program of China (2016YFA0301902). Y. X. acknowledges in addition support from the National Thousand-Young-Talents Program.

H.-X.Y. and T.T. contributed equally to this work.

APPENDIX: NUMERICAL CALCULATION METHOD AND COMPARISON WITH MEAN-FIELD-FLUCTUATION THEORY

In the text, we have calculated the quench dynamics of the system by exactly diagonalizing the many-body Hamiltonian, (2), in the Fock basis $|N_+, N_0, N_-\rangle = |n, N-2n, n\rangle$, where $n = 0, 1, \ldots, [N/2]$, with N being the number of atoms. In this Appendix, we compare the exact numerical result with the mean-field theory that takes into account the quantum fluctuations in the initial state. We see that they agree pretty well on short-time dynamics but deviate with a long evolution time or near the phase transition point.

The mean-field theory is described by the equations [19]

$$\begin{aligned}\dot{\rho}_0 &= \frac{2c_2}{\hbar}\rho_0\sqrt{(1-\rho_0)^2-m^2}\sin\theta,\\ \dot{\theta} &= -\frac{2q}{\hbar}+\frac{2c_2}{\hbar}(1-2\rho_0)\\ &\quad+\frac{2c_2}{\hbar}\frac{(1-\rho_0)(1-2\rho_0)-m^2}{\sqrt{(1-\rho_0)^2-m^2}}\cos\theta,\end{aligned} \tag{A1}$$

where $m = \rho_1 - \rho_{-1}$ denotes the magnetization and $\theta = \theta_1 + \theta_{-1} - 2\theta_0$ denotes the relative phase between spinors, with θ_ν ($\nu = 0, \pm 1$) representing the phase of each component. Clearly, with the initial state being a polar state with $\rho_0 = 1$ and $\rho_{\pm 1} = 0$, we cannot find any dynamics of ρ_0 during the time evolution. Here we consider a scenario where the spin-mixing dynamics is introduced by quantum fluctuations of the initial Fock state [28]. We follow the procedure in Ref. [28] to calculate time evolutions of ρ_0. We define a rank 2 nematic tensor $\hat{Q}_{ij} = \hat{S}_i\hat{S}_j + \hat{S}_j\hat{S}_i - (4/3)\delta_{ij}$, with $i, j \in \{x, y, z\}$ and δ_{ij} being the Kronecker delta. Here $\hat{S}$ is the spin operator. It can be found that $\hat{S}_x$, $\hat{S}_y$, $\hat{Q}_{xz}$, and $\hat{Q}_{yz}$ have an expectation value of 0 and a variance of N in the initial state $|N_1, N_0, N_{-1}\rangle = |0, N, 0\rangle$. Let us further write ρ_0, m, and θ as a function of these quantities [28],

$$\begin{aligned}\rho_0 &= \frac{1}{2}+\frac{1}{2}\sqrt{1-\frac{1}{2}\left[\left(\frac{S_x+Q_{xz}}{\cos\chi_+}\right)^2+\left(\frac{S_x-Q_{xz}}{\cos\chi_-}\right)^2\right]},\\ m &= \frac{1}{8\rho_0}\left[\left(\frac{S_x+Q_{xz}}{\cos\chi_+}\right)^2-\left(\frac{S_x-Q_{xz}}{\cos\chi_-}\right)^2\right],\\ \tan\chi_+ &= -\frac{S_y+Q_{yz}}{S_x+Q_{xz}},\\ \tan\chi_- &= \frac{S_y-Q_{yz}}{S_x-Q_{xz}},\end{aligned} \tag{A2}$$

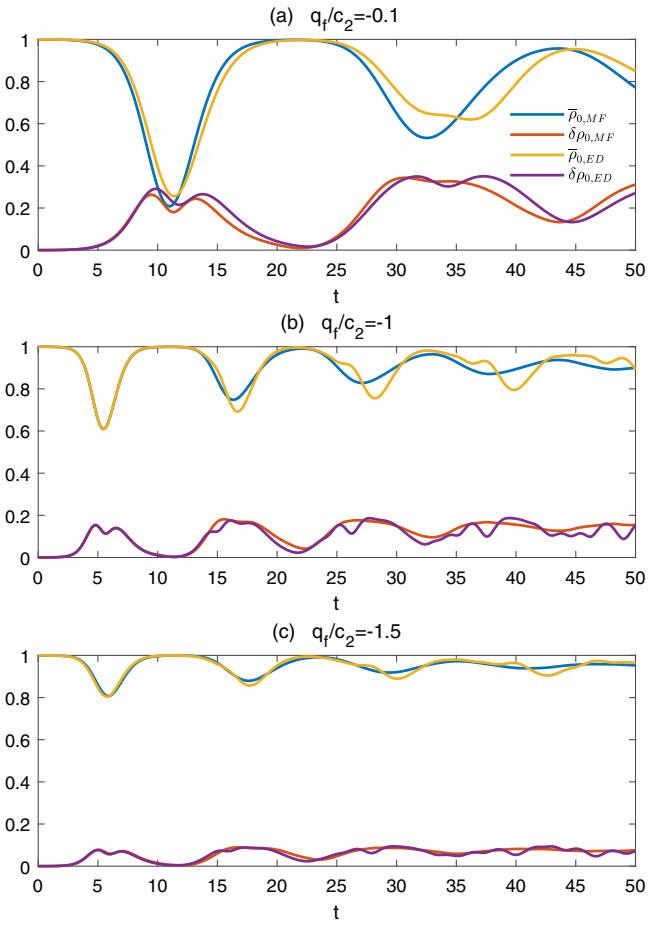

FIG. 6. Time evolution of $\overline{\rho}_0$ and $\delta\rho_0$ for three q_f/c_2 values starting from an LP state of 1×10^4 sodium atoms. From top to bottom, q_f/c_2 equals 0.1, −1, and −1.5, respectively. We use two simulation methods for calculation: through mean-field theory accompanied by quantum fluctuation, labeled with subscript "*MF*"; and through exact diagonalization of the model Hamiltonian, labeled with subscript "*ED*". When $q_f/c_2 = -1$ and −1.5, the two approaches give almost the same results in the first oscillation period, while they show deviations from the beginning when $q_f/c_2 = -0.1$. Time is in units of $2\pi\hbar/c_2$.

where $\chi_\pm = \theta_{\pm 1} - \theta_0$, leading to $\theta = \chi_+ + \chi_-$. To induce the quantum fluctuations in the initial state, we randomly generate values of S_x, S_y, Q_{xz}, and Q_{yz} based on normal distributions, with their expectation values and variance being 0 and N, respectively, and then substitute them into Eq. (A2) to obtain ρ_0, θ, and m. Using these quantities as the initial condition, we solve Eqs. (A1) to obtain the time-evolved ρ_0. By repeating 10^4 configurations for the initial state, we obtain the mean value and standard deviation of $\rho_0(t)$ for several values of q_f, as shown in Fig. 6. This semiclassical model predicts that spin-mixing oscillations can occur even for an initial state of $\rho_0 = 1$.

In Fig. 6, we plot the time-evolved $\overline{\rho}_0(t)$ and $\delta\rho_0(t)$ (standard deviation of ρ_0) obtained by these two methods. Their comparison illustrates that the results calculated by the mean-field method qualitatively agree with the exact results, in particular, in the short-time region $t \lesssim \tau_{\rm dip}$, while they show a significant difference in the longer-time region. In Fig. 7, we further compare their short-time characteristics ($A_{\rm dip}$, $\tau_{\rm dip}$, $\delta\rho_0$ at $t = \tau_{\rm dip}$) as a function of q_f/c_2. This indicates that the predictions of these two methods coincide when $q_f/c_2 \approx -1$, while they deviate near the dynamical phase transition point $q_f = 0$. Based on these findings, we conclude that the semiclassical approach (mean-field theory accompanied by initial quantum fluctuations) captures the major physics of the observed short-time quench dynamics except for the region around the phase transition point.

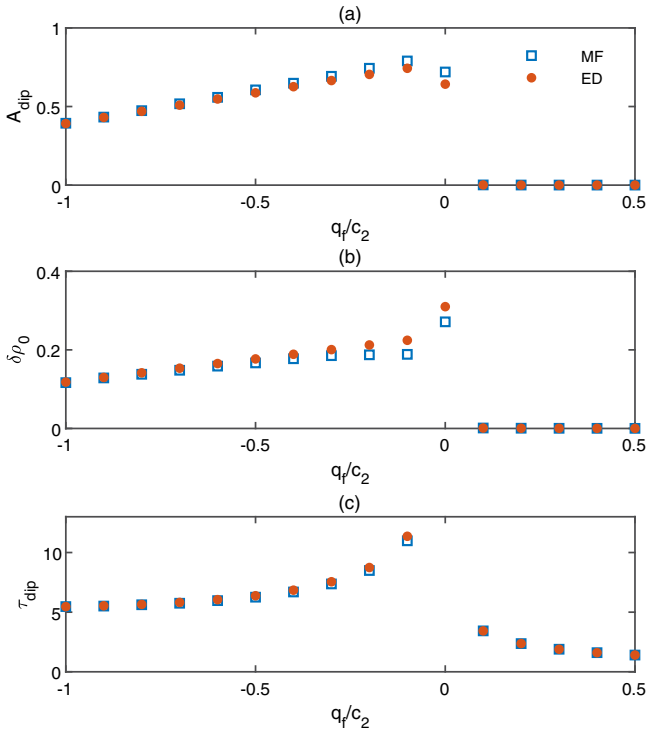

FIG. 7. Short-time properties (a) $A_{\rm dip}$, (b) $\delta\rho_0$ at $t = \tau_{\rm dip}$, and (c) $\tau_{\rm dip}$ as a function of q_f/c_2, obtained through the mean-field theory accompanied by quantum fluctuations in initial states (blue squares) and exact diagonalization (red circles) of model Hamiltonian (2).

[1] A. Polkovnikov, K. Sengupta, A. Silva, and M. Vengalattore, Rev. Mod. Phys. **83**, 863 (2011).
[2] M. Heyl, Rep. Prog. Phys. **81**, 054001 (2018).
[3] B. Sciolla and G. Biroli, Phys. Rev. Lett. **105**, 220401 (2010).
[4] A. A. Zvyagin, Low Temp. Phys. **42**, 971 (2016).
[5] M. Heyl, A. Polkovnikov, and S. Kehrein, Phys. Rev. Lett. **110**, 135704 (2013).
[6] B. Žunkovič, M. Heyl, M. Knap, and A. Silva, Phys. Rev. Lett. **120**, 130601 (2018).
[7] M. Heyl, Phys. Rev. Lett. **113**, 205701 (2014).
[8] P. Jurcevic, H. Shen, P. Hauke, C. Maier, T. Brydges, C. Hempel, B. P. Lanyon, M. Heyl, R. Blatt, and C. F. Roos, Phys. Rev. Lett. **119**, 080501 (2017).
[9] V. Gurarie, arXiv:1806.08876.
[10] N. Fläschner, D. Vogel, M. Tarnowski, B. S. Rem, D.-S. Lühmann, M. Heyl, J. C. Budich, L. Mathey, K. Sengstock, and C. Weitenberg, Nature Phys. **14**, 265 (2018).
[11] P. Titum, J. T. Iosue, J. R. Garrison, A. V. Gorshkov, and Z.-X. Gong, arXiv:1809.06377.
[12] J. Zhang, G. Pagano, P. W. Hess, A. Kyprianidis, P. Becker, H. Kaplan, A. V. Gorshkov, Z.-X. Gong, and C. Monroe, Nature **551**, 601 (2017).
[13] H. Bernien, S. Schwartz, A. Keesling, H. Levine, A. Omran, H. Pichler, S. Choi, A. S. Zibrov, M. Endres, M. Greiner, V. Vuletić, and M. D. Lukin, Nature **551**, 579 (2017).
[14] Y. Kawaguchi and M. Ueda, Phys. Rep. **520**, 253 (2012).
[15] D. M. Stamper-Kurn and M. Ueda, Rev. Mod. Phys. **85**, 1191 (2013).
[16] C. S. Gerving, T. M. Hoang, B. J. Land, M. Anquez, C. D. Hamley, and M. S. Chapman, Nat. Commun. **3**, 1169 (2012).
[17] Z. Zhang and L. M. Duan, Phys. Rev. Lett. **111**, 180401 (2013).
[18] C. B. Dağ, S.-T. Wang, and L.-M. Duan, Phys. Rev. A **97**, 023603 (2018).
[19] W. Zhang, D. L. Zhou, M.-S. Chang, M. S. Chapman, and L. You, Phys. Rev. A **72**, 013602 (2005).
[20] Y. Liu, E. Gomez, S. E. Maxwell, L. D. Turner, E. Tiesinga, and P. D. Lett, Phys. Rev. Lett. **102**, 225301 (2009).
[21] E. M. Bookjans, A. Vinit, and C. Raman, Phys. Rev. Lett. **107**, 195306 (2011).
[22] J. Jiang, L. Zhao, M. Webb, N. Jiang, H. Yang, and Y. Liu, Phys. Rev. A **88**, 033620 (2013).
[23] C. Käfer, R. Bourouis, J. Eurisch, A. Tripathi, and H. Helm, Phys. Rev. A **80**, 023409 (2009).
[24] L. Zhao, J. Jiang, T. Tang, M. Webb, and Y. Liu, Phys. Rev. A **89**, 023608 (2014).
[25] J. Jiang, L. Zhao, M. Webb, and Y. Liu, Phys. Rev. A **90**, 023610 (2014).
[26] F. Gerbier, A. Widera, S. Fölling, O. Mandel, and I. Bloch, Phys. Rev. A **73**, 041602(R) (2006).
[27] M. Heyl, Phys. Rev. Lett. **115**, 140602 (2015).
[28] C. D. Hamley, C. S. Gerving, T. M. Hoang, E. M. Bookjans, and M. S. Chapman, Nature Phys. **8**, 305 (2012).